


Toward general regime maps for cohesive-particle flows: Force versus energy-based descriptions and relevant dimensionless groups

W. Casey Q. LaMarche^{1,2}  | Peiyuan Liu^{1,3} | Kevin M. Kellogg^{1,4} | Aaron M. Lattanzi^{1,5} | Christine M. Hrenya¹

¹Department of Chemical and Biological Engineering, University of Colorado, Boulder, Colorado, USA

²Particulate Solid Research Inc., Chicago, IL

³Pfizer Inc., Groton CT

⁴The Dow Chemical Company, Lake Jackson, TX

⁵Department of Mechanical Engineering, University of Michigan, Ann Arbor, MI

Correspondence

Christine M. Hrenya, Department of Chemical and Biological Engineering, University of Colorado, Boulder, CO, USA.
Email: hrenya@colorado.edu

Funding information

Dow Chemical Company; National Science Foundation, Grant/Award Numbers: ACI-1532236, ACI-1532235

Abstract

Much confusion exists on whether force- or energy-based descriptions of cohesive-particle interactions are more appropriate. We hypothesize a force-based description is appropriate when enduring-contacts dominate and an energy-based description when contacts are brief in nature. Specifically, momentum is transferred through force-chains when enduring-contacts dominate and particles need to overcome a cohesive force to induce relative motion, whereas particles experiencing brief contacts transfer momentum through collisions and must overcome cohesion-enhanced energy losses to avoid agglomeration. This hypothesis is tested via an attempt to collapse the dimensionless, dependent variable characterizing a given system against two dimensionless numbers: A generalized bond number, Bo_G -ratio of maximum cohesive force to the force driving flow, and a new Agglomerate number, Ag -ratio of critical cohesive energy to the granular energy. A gamut of experimental and simulation systems (fluidized bed, hopper, etc.), and cohesion sources (van der Waals, humidity, etc.), are considered. For enduring-contact systems, collapse occurs with Bo_G but not Ag , and vice versa for brief-contact systems, thereby providing support for the hypothesis. An apparent discrepancy with past work is resolved, and new insight into Geldart's classification is gleaned.

KEYWORDS

fluidization, mathematical modeling, multi-phase flow, multiscale modeling, particle technology

1 | INTRODUCTION

Agglomeration due to short-range, attractive forces between particles is critical to a range of phenomena that span length scales from the planetary to the molecular: formation of the universe,¹ asteroid strength,² industrial operations involving solid particles,³ droplet coalescence,⁴ colloid deposition,⁵ and atomic aggregation.⁶ For flows involving cohesive, solid particles, empirical correlations are known to be unreliable. For example, predictions of entrainment,⁷ transport disengagement height,⁸ and the size of fluidized agglomerates⁹ vary by an order of magnitude or more when applied to the same system.

The state-of-the-art for predicting the behavior of cohesive-particle flows is via regime maps.^{10–16} One of the earliest and most prolific examples is Geldart's empirical chart of fluidization regimes,¹⁰ with thousands of citations to date¹⁷ despite the lack of significant physical insight. Namely, Geldart's dimensional chart of density difference versus particle size is system-specific (gas–solid fluidized bed), operating-condition specific (ambient conditions), and cohesion-source specific (van der Waals forces).¹⁰ Some physical insight was shed on this empirical classification by showing that the demarcation of regimes can be recast based on the bond number—that is, the ratio of maximum particle-particle cohesive force (F_{max}) to particle

weight.^{11,18} Put another way, the system behavior (macroscopic) was mapped based on particle–particle cohesion levels (microscopic).

Following this preliminary insight, others attempted the micro–macro link in other cohesive systems via dimensionless regime maps based on F_{\max} .^{9,11–15,19,20} The resulting regime maps perform well for the specific systems and cohesion sources for which they were developed, for example, predicting the segregation of wet solids in rotating tumblers.¹³ Nonetheless, evidence suggests that application to other cohesion sources may be inappropriate. For instance, the link between fluidization behavior and bond number observed for van der Waals cohesion¹¹ does not extend to condensed-capillary (humidity-induced) cohesion.²¹ Hence, uncertainty remains regarding the applicability of previous regime maps to sources of cohesion different than those used to generate the maps (van der Waals, liquid bridges, etc.).

Here, we seek a more general (and thus more universal) dimensionless group, in which the numerator characterizes particle–particle cohesion and the denominator characterizes the corresponding quantity that acts in opposition (e.g., shear force). Hence, the numerator depends on the source of cohesion (van der Waals, capillary, etc.) while the denominator depends on the specific system considered (sheared, vibrated, etc.). Regarding the numerator, the overwhelming majority of past regime maps have been based on F_{\max} . Nonetheless, the cohesive energy can also be used to quantify the cohesion between particles—that is, particles agglomerate when their relative kinetic energy (KE) is smaller than the critical value of cohesive energy KE_{crit} .²² and confusion remains as to which quantity is more relevant in a given situation. For example, numerous estimates for agglomerate size in fluidized systems have been put forth, some of which are based on force balances and others based on energy balances.⁹ Further, agglomeration levels have been linked to the cohesive force in some systems²³ and the cohesive energy in others.^{24,25} Moreover, even in the same system, the macro-scale behavior has been linked to both F_{\max} and KE_{crit} . For instance, the flow behavior of a fluidized bed was recently linked to KE_{crit} for condensed-capillary cohesion,²¹ but was previously linked to F_{\max} for van der Waals forces.¹¹ Finally, the transition of wet solids in a vibrated bed from granular-gas to fluidized-grains was shown to be energy-driven, whereas the transition from a solid-like bed to fluidized was shown to be force-driven.²⁶ Though these previous works indicate that the macro-scale behavior was linked successfully to F_{\max} in some cases and KE_{crit} in others, it is not clear *a priori* which is more appropriate and why such a distinction exists.

In this work, we resolve the aforementioned discrepancies of cohesive-particle systems via a unifying physical understanding which links the macroscopic (system) behavior to microscopic (particle–particle) interactions. This micro–macro link is demonstrated via experiments and simulations of solids experiencing cohesion from different sources and in a variety of systems that span a range of particle concentrations. Specifically, universal behavior (collapsing of dimensionless plots) is observed using a ratio of forces—the generalized bond number Bo_G —for systems dominated by enduring contacts (“dense”) and a ratio of energies—the new Agglomerate number Ag —for systems dominated by brief contacts or collisions (“dilute”).

The numerators of the dimensionless groups depend on the magnitude and type of particle–particle cohesion (microscopic); the denominators characterize the relevant driving force or source of granular energy in the system and thus, unlike the numerators, are system-dependent. A key aspect of this work is the careful attention paid to estimating the denominator of Ag for each system. Our results support a new physical picture in which Bo_G dominates in enduring-contact systems, where momentum is transferred via force chains, and Ag dominates in brief-contact systems, where the flow is dominated by dissipative collisions. Moreover, we contend that Geldart's force-based classification of fluidized, cohesive solids¹⁰ is more appropriately based on a ratio of energies.

2 | DEVELOPMENT OF DIMENSIONLESS GROUPS

2.1 | Numerator considerations: Force versus energy

Particle–particle cohesion is often characterized by one of two quantities: the force required to separate surfaces in contact, F_{\max} , or the cohesive potential energy, W .²⁷ W is the integral of the cohesive force F_c (van der Waals, capillary force, etc.) over the separation distance x ,

$$W = \int_0^{x_{\max}} F_c(x) dx, \quad (1)$$

where the direction of x and F_c is between particle centers, and x_{\max} is effectively the maximum distance over which the force acts, i.e., x_{\max} is set to a finite approximation (that depends on cohesion source) for purposes of practicality and without undue loss of accuracy. The kinetic energy KE is defined as $KE = 0.5 mv^2$, where m is the reduced particle mass and v is the normal component (taken in the direction between particle centers) of the relative particle velocity. Figure 1 illustrates F_c and kinetic energy KE profiles for cohesive particles before and after a collision. As shown in Figure 1A, F_c is unaffected by the collisional process. However, even for non-cohesive particles, a fraction of KE is dissipated during the collision due to its inelastic and/or frictional nature. For cohesive particles, additional energy is lost due to the acceleration of the approaching particles in the cohesive-force field, which leads to a higher impact velocity at contact. As shown in Figure 1B, such dissipation leads to a hysteresis in KE . Based on the initial KE and the amount of dissipation (Figure 1B), the particles may fully separate after collision (dashed-blue line) or agglomerate (solid-blue line). For frictionless particles, the final KE of separating particles with normal, relative pre-collisional velocity v_i is $KE_f = 0.5 mv_f^2 = e^2(0.5 mv_i^2 + W) - W$, where e is the restitution coefficient and v_f is the normal, relative post-collisional velocity.²⁸ KE_f accounts for both non-contact (W) and collisional (e) losses in KE . The demarcation between agglomeration and separation occurs at

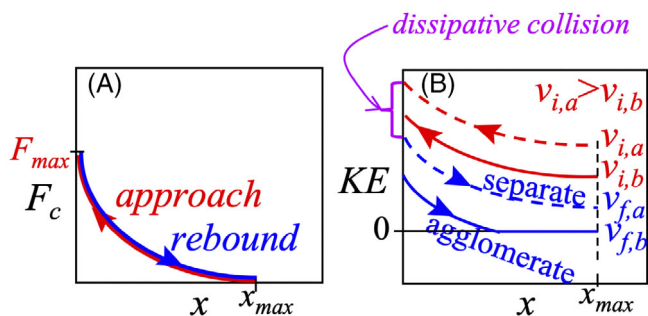


FIGURE 1 Force (A) and kinetic energy (B) profiles for the approach, collision, and rebound of two cohesive particles. (A) The cohesive force F_c depends only on separation distance x so no hysteresis occurs. (B) Dissipation of KE during collision of particles leads to hysteresis. Dashed and solid lines illustrate two scenarios that depend on initial KE and/or level of dissipation during the collision. The dashed lines represent particle pair a that have a high enough initial KE ($0.5v_{i,a}^2 > 0.5v_{crit}^2$) to fully separate (no agglomerate forms). The solid lines represent particle pair b that do not have a sufficiently high initial KE ($0.5v_{i,b}^2 \leq 0.5v_{crit}^2$) to avoid agglomeration [Color figure can be viewed at wileyonlinelibrary.com]

$KE_f = 0$, and can be quantified by the critical agglomeration velocity, v_{crit} —the minimum, relative (normal), pre-collisional velocity required to avoid agglomeration. The analytical solution for v_{crit} between inelastic, hard spheres is²²

$$v_{crit} = (2W(1 - e^2)/(me^2))^{1/2}. \quad (2)$$

Here we use $KE_{crit} = 0.5mv_{crit}^2$, rather than W , to quantify the cohesive energy, as collisional losses of KE play a role in whether or not agglomeration occurs. To underscore the importance of dissipation, note that elastic particles ($e = 1$) always separate due to the absence of dissipation (pre-collision velocity = post-collision velocity), and thus will never agglomerate ($v_{crit} = 0$).

2.2 | Dimensionless groups (Bo_G and Ag)

To determine whether force or energy considerations are more appropriate for a given system, we will examine plots below of the relevant dependent variable for a given system (e.g., degree of agglomeration) versus the level of cohesion. The level of cohesion will be represented by one of two dimensionless groups, one based on force and the other based on energy. F_{max} and KE_{crit} , which form the numerators of the respective dimensionless groups, depend on the type of cohesion (van der Waals, etc.) and material properties. The denominators are the system-dependent, characteristic force (F_{sys}) and granular energy ($\theta_{fluc,sys}$) driving the flow in the system (described in detail below). Namely, we utilize a generalized Bond number, Bo_G , which is the ratio of F_{max} to the characteristic force driving particle motion, F_{sys} :

$$Bo_G = F_{max}/F_{sys}. \quad (3)$$

We further define a new Agglomerate number, Ag , as the ratio of KE_{crit} to the characteristic granular energy $\theta_{fluc,sys}$ ($\theta_{fluc,sys} = 3mT_{sys}/2$, where the granular temperature is $T_{sys} = \langle v'^2 \rangle / 3$ and v' is the particle velocity relative to the local mean solids velocity):

$$Ag = KE_{crit}/\theta_{fluc,sys} = v_{crit}^2/3T_{sys}. \quad (4)$$

It is worthwhile to note that F_{max} and KE_{crit} , which form the numerators of the two dimensionless groups, depend on the type of cohesion (van der Waals, etc.) and material properties. The denominators (F_{sys} and T_{sys}), however, are system dependent, as elaborated on below. Physically, the dimensionless numbers represent a competition between the effects of particle–particle cohesion and the ability of the system to overshadow those effects; small values of Bo_G and Ag indicate relatively low levels of cohesion and vice versa.

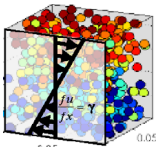
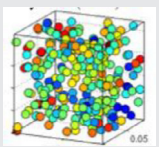


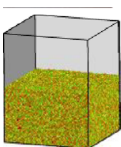

2.3 | Denominator considerations: Dependence on system

Further comment on our choices for the denominators of the two dimensionless groups, and how it relates to past work, is warranted. Namely, particle weight is often used as the denominator^{9,11,12,19,20} for dimensionless groups that utilize a cohesive force in the numerator, though often the physical basis of such a choice is not provided. Accordingly, we choose a more general form of the denominator—that is, the characteristic force driving the motion (F_{sys}). Since dimensionless groups involving KE_{crit} in the numerator are much less common in past works, the denominator has not been explored as extensively. As noted previously,²⁴ the kinetic energy of fluctuating particle velocities (or granular energy, $\theta_{fluc,sys}$) is related to the particle impact velocity and hence is relevant to agglomeration; that is, for impact velocities below v_{crit} , agglomeration occurs, and vice versa (Figure 1B). However, unlike the particle weight oft used in force-based groups, estimating the characteristic granular energy *a priori* is nontrivial.⁹ This challenge may explain why the *mean* kinetic energy was often used in the denominator even though the kinetic energy of *fluctuating* particle motion was previously identified as the relevant choice.^{26,29} Unlike $\theta_{fluc,sys}$, the *mean* energy of the system is representative of the average velocity of all particles, and therefore does not directly affect agglomeration.

3 | METHODS

As alluded to above, the appropriateness of a force- or energy-based description of cohesion will be tested via the collapse of plots based on Bo_G or Ag , respectively. To ensure robustness of the results, the dimensional quantities contained in Bo_G and Ag must be systematically varied. We accomplished this via experiments and simulations of particles experiencing cohesion from different sources (numerators)

TABLE 1 Overview of the systems considered [Color table can be viewed at wileyonlinelibrary.com]

System	Regime	DEM or experiment	Sources of cohesion	Bo_G	Ag
SSF 	Dilute	DEM	Square-force, humidity and van der Waals	$Bo_{G,SSF} = F_{max}/\rho_p^2 d^4$	$Ag_{SSF} = v_{crit}^2/3\gamma^2 d^2$
HCS 	Dilute	DEM	Square-force, humidity and van der Waals	$Bo_{G,HCS} = F_{max}/(T_0\rho_p d^2/\tau^2)$	$Ag_{HCS} = v_{crit}^2/(3T_0/\tau^2)$
Riser 	Dilute	DEM	Square-force, humidity and van der Waals	$Bo_{G,Riser} = F_{max}/\rho_t U_t^2 d^2$	$Ag_{Riser} = v_{crit}^2/3U_t^2$
BB 	Dilute	Experiment	Humidity and van der Waals	$Bo_{G,BB} = F_{max}/mg$	$Ag_{BB} = v_{crit}^2/(3dg)$
PB 	Dense	DEM	Square-force	$Bo_{G,PB} = F_{max}/mg$	N/A
PB 	Dense	Experiment	Humidity and van der Waals	$Bo_{G,PB} = F_{max}/mg$	N/A
Hopper 	Dense	DEM	Square-force, humidity and van der Waals	$Bo_{G,Hopper} = F_{max}/mg$	$Ag_{Hopper} = v_{crit}^2/(3dg)$

Abbreviations: BB, bubbling bed; DEM, discrete element method; HCS, homogenous cooling system; PB, packed bed; SSF, simple shear flow.

and in a variety of systems (denominators). We also considered systems with a wide range of concentrations, in order to test our hypothesis that enduring-contact or “dense” flows are dictated by force considerations and brief-contact or “dilute” flows are dictated by energy considerations. It is worth noting that the dense and dilute classifications defined here are used for conciseness to refer to the nature of contacts only—enduring versus brief, respectively.

The experiments and soft-sphere discrete element method (DEM) simulations used here are fairly standard and have been documented in our previous publications. For sake of brevity, the details on the

experimental and simulation methods are relegated to the supplementary information (Supp Sec S1–S4). Specifics on the types of cohesion (which affect the numerator of Bo_G and Ag) and systems (denominator of Bo_G and Ag) considered here are detailed below; an overview is provided in Table 1.

3.1 | Sources of cohesion considered (numerator)

We consider cohesion arising from three sources: (i) van der Waals interactions, (ii) capillary bridges formed by condensation (humidity),

TABLE 2 Equations for solving the condensed capillary force

Description	Equation
Capillary force, ³⁹	$F_{RH} = 2\pi a_2 \sigma - \pi a_2^2 \eta_{RH} \ln(RH)$ (6)
Kelvin and Laplace-Young equations, ⁴⁰	$-\eta_{RH} \ln(RH) = \sigma(1/a_1 - 1/a_2)$ (7)
Bridge curvature, ⁴¹ a_1	$a_1 = r_s [(1 + x/2r_s) \sec(\beta) - 1]$ (8)
Bridge thickness, ⁴¹ a_2	$a_2 = r_s [(1 + x/2r_s)(\tan(\beta) - \sec(\beta)) + 1]$ (9)

(iii) and a “square-force” model.³⁰ These sources, detailed below, impact the values of F_{max} and v_{crit}^2 (numerators of Bo_G and Ag , respectively). Both experiments and DEM simulations are used to investigate sources (i) and (ii), and only DEM is used for (iii).

Though the values of F_{max} and v_{crit}^2 are determined based on a given source of cohesion as described below, a few commonalities are worth noting. For both simulations and experiments, F_{max} occurs at the minimum separation distance, x_{min} , (and $F_c(x \leq x_{min}) = F_{max}$) which is specific to the cohesion source. For experiments, the glass particles used are approximately rigid (relatively-high Young’s modulus E) and therefore we use the (hard-sphere) Equation (2) for v_{crit}^2 ; see Supp Sec S1 for details on experiments and Supp Sec S2 for details on the particles. For simulations, softer particles (smaller E) were used and thus v_{crit}^2 was determined from simulations of two-particle collisions (Supp Sec S3) using the force expression $F_c(x)$ for each cohesion source as described below. The Young’s modulus used in different simulations ranged from 1 to 10^4 MPa. Since the current work is not intended for directly comparing simulation results against experiments, Young’s moduli smaller than that of glass particles ($E = 7.3 \times 10^4$ MPa)³¹ were used in simulations to vary v_{crit}^2 independently of F_{max} .^{32–34} For further details on the particles used in simulations, see Supp S4.

(i) *van der Waals cohesion*—A van der Waals theory validated for the glass particles used in the experiments^{35,36} was used to determine F_{max} and v_{crit}^2 in both experiments and simulations. The cohesive force for two, rough spheres with radius R is given by a “submerged-sphere” model with two scales of roughness:³⁵

$$F_{vdW} = \frac{A}{6} \left[\frac{R}{2(x+2h_l+2h_s)^2} + \frac{2Rr_l}{(R+r_l)(x+h_l+2h_s)^2} + \frac{2Rr_s}{(R+r_s)(x+h_l+h_s)^2} + \frac{r_l}{2(x+2h_s)^2} + \frac{2r_l r_s}{(r_l+r_s)(x+h_s)^2} + \frac{r_s}{2x^2} \right], \quad (5)$$

where A is the Hamaker constant, r_s is the small-scale asperity radius, h_s is the small-scale asperity height, r_l is the large-scale asperity roughness, and h_l is the large-scale asperity height. A detailed explanation of the submerged sphere method and the modeling of surface via two scales of roughness is available elsewhere.^{35,37,38} Our prior work has demonstrated that the two-scale roughness model works well for the glass beads used here, in which two scales of roughness are clearly evident from AFM-based surface maps.^{35,36} For both experiments and

simulations, F_{max} is determined via Equation (5) as $F_{max} = F_{vdW}(x_{min})$, where an intermolecular distance of 0.3 nm is used for x_{min} , thereby precluding an infinite force at contact. For both experiments and simulations, x_{max} is set to 400 nm in order to determine v_{crit}^2 (via Equations (1), (2), and (5) for experiments, and via two-particle DEM simulations for many-particle simulations), which is large enough to not affect v_{crit}^2 appreciably as F_{vdW} decreases asymptotically with increasing x .²⁷ Equation (5) was also used to determine the van der Waals force as a continuous function of separation distance in the many-particle DEM simulations (along with the particle surface roughness values measured for our experimental materials, which are provided in Table S1 of the supplemental material).

To systematically vary the van der Waals cohesion level, different values of F_{max} and v_{crit} (numerators of Bo_G and Ag , respectively) were achieved by changing A in simulations and utilizing different-sized particles in the experiments and simulations (details in Supp Sec S2 and S4).

(ii) *Condensed-capillary cohesion*—The condensed-capillary cohesive force (F_{RH}) is determined by solving the system of equations provided in Table 2, where RH is relative humidity, σ is surface tension, and η_{RH} is the product of ambient air temperature, ideal gas constant and molar density of water; the accuracy and assumptions used for calculating F_{RH} are discussed elsewhere.^{27,42}

In the presence of humidity, small bridges can condense between particles at small separation distances x . The magnitude of the cohesive force of the bridge is related to the thickness (a_2) and curvature (a_1) of the bridge, which are found as a function of the half-filling angle β .⁴¹

Similar to the van der Waals force, surface roughness of the particles directly influences the magnitude of F_{RH} as the liquid bridge condenses between surface asperities. Our previous work showed that the liquid bridge is likely condensing between the small-scale asperities, and hence the bridge curvature and thickness depend on the small-scale asperity radius r_s in Equations (8) and (9) (Table 2).²¹ To solve for the condensed capillary force F_{RH} (Equation (6) in Table 2), the half-filling angle β (Equations (8) and (9) in Table 2) is calculated for a given η_{RH} (Equation

(7)), RH (Equation (7)), and x (Equations (8) and (9)). β is then used to determine the capillary bridge thickness a_2 (Equation (9)), which is needed to find the condensed capillary force F_{RH} (Equation (6)).

This iterative process was used to calculate F_{RH} in order to determine F_{max} and v_{crit}^2 for experiments and simulations. In particular, similar to F_{vdw} , a non-zero x_{min} (intermolecular distance = 0.3 nm) is required for the vapor molecules to condense into a (liquid) bridge between particles.⁴³ Accordingly, $F_{max} = F_{RH}(x_{min})$ is used for both experiments and simulations. x_{max} , which is needed to determine v_{crit}^2 (Equation (2)), is solved numerically by setting $F_{RH} = 0$ for the system of equations in Table 2. (For the reader interested in a simpler representation of the relationship between variables, a good approximation of x_{max} is $x_{max} \approx 2\sigma/(\gamma_{RH} \ln(RH))$ with details discussed elsewhere.⁴⁴)

In order to vary the level of condensed-capillary cohesion, the magnitude of F_{max} and v_{crit} (numerators of Bo_G and Ag , respectively) were altered by varying the RH in the experiments and simulations.

(iii) *Square-force model*—The square-force model³⁰ has similarities to the well-known square-well model,⁴⁵ with the key difference being that the cohesive force, rather than the potential energy, is held constant over a short distance from the particle surface, and is zero beyond. Namely, the square-force model is given by,

$$F_{sf}(x) = \begin{cases} F_{max}, & x \leq x_{max} \\ 0, & x > x_{max} \end{cases}, \quad (10)$$

where F_{max} is the constant force that acts over the distance x_{max} from particle surface.

While no physical analog to the square-force model exists, this model allows F_{max} and v_{crit}^2 to be controlled independently. Specifically, the cohesive force can be changed while keeping the cohesive energy constant, and vice versa, thereby allowing a clean test as to whether a force- or energy-based approach is more appropriate for a given system. For example, to keep the force fixed while varying the energy, various x_{max} values are used for the same F_{max} , resulting in different values for W (and hence v_{crit}^2) for each x_{max} (see Equations (1) and (2)). The square-force model is only used in DEM simulations and therefore the value of v_{crit}^2 is determined from two-particle simulations as described above and in the supplemental material (Supp Sec. S3).

To systematically vary the level of cohesion in simulations utilizing a square-force model, systems with the same cohesive force (F_{max}) but different cohesive energy (numerators of Bo_G and Ag , respectively) are examined. Specifically, F_{max} and x_{max} are used as controllable input parameters in $F_{sf}(x)$ (Equation (10)).

3.2 | Systems examined (denominator)

Similar to varying the numerators of Bo_G and Ag by changing cohesion sources and their magnitude (Section 3.1), we also varied the denominators by examining different systems. For Bo_G , determining the denominator (characteristic force driving particle motion; see Equation (3)) is typically more straightforward than for Ag (characteristic granular energy; see Equation (4)). For the latter, we take the

following approach for each system enumerated below: we identify the source of granular temperature (or equivalently granular energy) and estimate its dependency on input parameters. Additionally, the dependent variable (measured or predicted) that we are seeking collapse for is identified below for each system. The dependent variables chosen are necessarily different due to the wide range of systems examined—that is, the dependent variable in one system may be an input for another (e.g., porosity is an output of the packed bed system but an input to riser flow) and/or the dependent variable in one type of system is non-trivial to define in another (e.g., identifying agglomerates in packed bed). Pictures of the systems are provided in Table 1.

(i) *Simple shear flow (SSF)*—In simulations of SSF, a constant velocity gradient is imposed in one direction.⁴⁶ The steady-state fraction of particles in agglomerates (N_{agg}/N_{tot} , where N_{agg} is the number of particles in agglomerates and N_{tot} is the total number of primary particles) is the dependent variable, which will be plotted against Bo_G and Ag for various cohesion levels. First considering the denominator of Bo_G (Equation (3)), the system-specific driving force for the SSF system is generated from the shear stress, which is proportional to $\rho_p \gamma^2 d^2$,^{46,47} where ρ_p is particle density, d is particle diameter and γ is shear rate. Since the ratio of system size, L , to d is kept constant during the simulations, the characteristic force driving flow is proportional to $\rho_p \gamma^2 d^4$ and thus we define F_{sys} as $\rho_p \gamma^2 d^4$. Accordingly, based on Equation (3):

$$Bo_{G,SSF} = F_{max}/\rho_p \gamma^2 d^4. \quad (11)$$

Next considering the denominator of Ag (Equation (4)), the source of $\theta_{fluc,sys}$ is also proportional to shear ($\propto \rho_p \gamma^2 d^2$),⁴⁸ and thus we define the characteristic temperature as $T_{sys} \equiv \gamma^2 d^2$. Then, according to Equation (4),

$$Ag_{SSF} = v_{crit}^2/3\gamma^2 d^2. \quad (12)$$

Several points are noteworthy. First, the numerators F_{max} and v_{crit}^2 depend on the cohesion source (Section 3.1), but are independent of system, so these quantities will appear in all numerators in this section. Second, subscripts are added to Bo_G and Ag to denote the system under consideration, since the denominators are system dependent. Third, note that it is the dependency of T_{sys} ($\theta_{fluc,sys}$) on system parameters (inputs)—rather than a specific estimate of this quantity—that is critical. In particular, the significance of specifying the dependence of T_{sys} on system inputs is important as the usefulness of dimensionless groups stems from a dependency on parameters that are known *a priori*—i.e., input parameters only (rather than local, continuum quantities). Hence, we *define* a characteristic T_{sys} as $T_{sys} \equiv f$ (system inputs) (using the symbol \equiv instead of $=$). Similarly, we define a characteristic force as $F_{sys} \equiv f$ (system inputs). This concept is illustrated further in the results (Section 4). These three comments are similarly applicable to each of the systems described below.

(ii) *Homogeneous cooling system (HCS)*—The HCS simulations are fully periodic with no mean motion or external forces. Thus, $\theta_{fluc,sys}$

decays with time.⁴⁹ We use Haff's law⁴⁹ ($T = T_0[1 + t\zeta_0(0)]^{-2}$ where t is time, T_0 is the initial granular temperature, and $\zeta_0(0)$ the initial cooling rate⁵⁰) to define $T_{sys} \equiv T_0/\tau^2$, where τ the dimensionless time $\tau = (1 + t\zeta_0(0))$. F_{sys} is the force resulting from the collisional stress (momentum transfer between colliding particles), which stems from granular pressure (p_s) in the HCS, namely $p_s = F_{sys}/a_s$. Based on the well-documented analogy with molecular gases, we use $p_s = \rho_p T_{sys}$ along with characteristic area $a_s = d^2$ to define $F_{sys} \equiv T_0 \rho_p d^2 / \tau^2$ (where the ratio of domain length to particle size, L/d , is kept constant for all simulations). Therefore, the HCS Agglomerate number is

$$Ag_{HCS} = v_{crit}^2 / (3T_0/\tau^2), \quad (13)$$

and the bond number of the HCS is

$$Bo_{G,HCS} = F_{max} / (T_0 \rho_p d^2 / \tau^2). \quad (14)$$

The level of agglomeration, N_{agg}/N_{tot} , is again the dependent variable of interest.

(iii) *Riser*—The riser is a dilute suspension of particles (solids volume fraction $\phi = 1\%$) entrained by upward-flowing gas in a fully periodic domain. The steady-state agglomeration level N_{agg}/N_{tot} is taken as the dependent variable. In a riser, the drag force drives the motion of the particles, and it is commonly described by $F_{drag} = (1/8)C_D \rho_f \pi d^2 (U - u_s)^2$ for single particles,⁵¹ where C_D is the coefficient of drag, U is the gas velocity and u_s is the solids velocity. We use the single particle terminal velocity U_t (a value that can be determined *a priori*) as an estimate for $U - u_s$. Accordingly, the system-specific driving force used here is $F_{sys} \equiv \rho_f d^2 U_t^2$ and thus the bond number for the riser is

$$Bo_{G,Riser} = F_{max} / \rho_f U_t^2 d^2, \quad (15)$$

where ρ_f is the gas density and the single-particle terminal velocity U_t is used to estimate the relative velocity between the phases. For our simulations (homogenous and uniform gas flow), $\theta_{fluc,sys}$ is generated via the interaction of neighbor particles through the fluid; this source is proportional to the slip velocity squared,⁵² that is, $T_{sys} \equiv U_t^2$. Hence, the riser Agglomerate number is given by:

$$Ag_{Riser} = v_{crit}^2 / 3U_t^2. \quad (16)$$

(iv) *Bubbling Bed (BB)*—Controlled sedimentation is achieved by incrementally lowering the gas velocity at the bottom of the bed (inlet) until the particles come to rest in a packed-bed state. Prior to each sedimentation run, the gas delivered to the bottom of the bed at a sufficiently high velocity to ensure the bed would be in a bubbling state. This initial gas velocity to ensure the particles were initialized in a bubbling bed (BB) was determined in our previous work.^{21,53} Thus, the BB is the (relatively dilute) starting point of our sedimentation system, and it was investigated experimentally.^{21,53} The minimum velocity associated with the presence of bubbles U_{mb} , normalized by the non-cohesive value U_{NC} ,^{42,53} is the dependent variable of interest.

When solids are fully fluidized in the bubbling state, the drag equals bed weight, and thus

$$Bo_{G,BB} = F_{max} / mg. \quad (17)$$

Although dilute (collision-dominated), the BB has a much higher concentration than the HCS and SSF, and thus we assume that motion of individual particles is $\sim d$ between collisions. Accordingly, the potential energy of the relative motion of particles (mgd) is used to define $T_{sys} \equiv 3dg$, and the Agglomerate number in the BB is thus

$$Ag_{BB} = v_{crit}^2 / (3dg). \quad (18)$$

(v) *Packed Bed (PB)*—In the dense, packed-bed (PB) limit of the sedimentation system, no gas flow occurs. The particles are stationary for several gas velocity set points prior to the no-gas-flow condition.⁵⁴ Hence, a granular energy does not exist. Bed compaction is caused by the gravitational forces on the particles, and thus F_{sys} is mg and the PB bond number is

$$Bo_{G,PB} = F_{max} / mg. \quad (19)$$

The porosity ($1 - \phi$) is the dependent variable of interest in both experiments and simulations. However, simulations and experiments are considered separately because DEM is limited to smaller beds and particles with a smaller Young's modulus (Section 3.1) than experiments.³⁴

(vi) *Hopper*—Simulated particles are discharged through a slit at the bottom of a hopper. The steady-state discharge rate of cohesive solids (D_c) is the dependent variable of interest and is normalized by the discharge rate of non-cohesive particles (D_{NC}). Gravity drives flow from the hopper, that is, $F_{sys} \equiv mg$, and thus the bond number of the hopper is

$$Bo_{G,Hopper} = F_{max} / mg. \quad (20)$$

Similar to the BB, the Agglomerate number of the hopper is

$$Ag_{Hopper} = v_{crit}^2 / (3dg), \quad (21)$$

because the hopper is dense (particle motion limited to $\sim d$) and T_{sys} is proportional to the potential energy associated with the relative particle motion.

4 | RESULTS AND DISCUSSION

Below we evaluate our hypothesis that a force-based description is more appropriate when enduring contacts dominate and an energy-based description is more appropriate when contacts are brief in nature. Namely, we use the wide range of experimental and simulation systems (fluidized bed, hopper flow, etc.) and cohesion sources (van der Waals, humidity, etc.) detailed above to determine if the dependent variables of dense systems collapse with Bo_G but not Ag , and vice versa for dilute systems.

4.1 | Validating T_{sys} (input) against T_{actual} (output)

Before testing for collapse with $Ag (=v_{\text{crit}}^2/3T_{\text{sys}})$, it is worthwhile to verify that a correct characteristic granular temperature (T_{sys}) was identified for each system based on input parameters alone. Recall that our approach, as detailed above, was to identify the source of granular temperature for each system, and then define T_{sys} such that it captured the dependency of this source on input parameters. As a quick gauge of the appropriateness of this approach, we can compare this characteristic T_{sys} based on input parameters to the actual granular temperature observed in the system. This is only straightforward to accomplish for DEM simulations, as experimental measurements of granular temperature are non-trivial at best. Further, because granular temperature is defined in terms of a fluctuation velocity, this comparison is most easily accomplished in systems with well-defined local, mean velocities—i.e., SSF (linear mean velocity) and HCS (zero mean velocity). The resulting comparison between the characteristic T_{sys} (based on input parameters) and the granular temperature T_{actual} extracted from simulations (output), is shown in Figure 2 for SSF and HCS (subplots A and B, respectively). T_{sys} and T_{actual} are only plotted in Figure 2 when the systems are not fully agglomerated (i.e., when $T_{\text{actual}} > 0$), because the definition of granular temperature becomes enigmatic when the systems are fully agglomerated. The nearly linear behavior indicates that the T_{sys} , identified as the source of granular temperature (denominator of Ag) is proportional to the measured value of the granular temperature T_{actual} except when the system $T_{\text{actual}} \sim 0$. Not surprisingly, the proportionality constant differs by ~ 1 order of magnitude between SSF and HCS, since T_{sys} is a characteristic temperature of a given system rather than an estimate of T_{actual} .

4.2 | Collapse of brief-contact (dilute) systems

Given the confidence in our approach for determining a characteristic temperature T_{sys} as described above, we are now well-positioned to begin evaluating our hypothesis that brief-contact (dilute) systems will collapse with Ag but not Bo_G . In particular, for a given system, we methodically changed not only the type of cohesion, but also other parameters appearing in the numerator and denominator of the

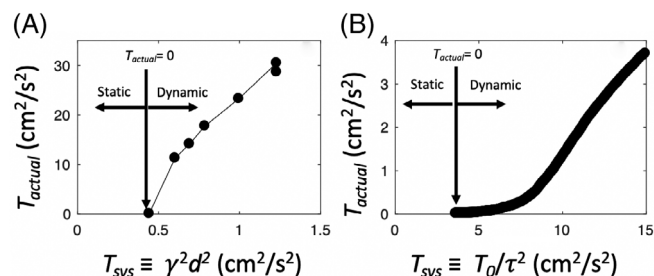


FIGURE 2 The source of T_{sys} identified in each system (plotted on x-axis) is proportional to the measured value T_{actual} (plotted on y-axis) for (A) simple shear flow (SSF) and (B) homogenous cooling system (HCS)

dimensionless groups in order to ensure robustness of any observed collapse. Figure 3 displays the results from the first system examined, namely SSF, in which the fraction of particles in agglomerates (dependent variable) is plotted against $Bo_{G,SSF}$ and Ag_{SSF} (independent variables) in subplots A and B, respectively. Each data point in these plots represent a different system condition. First, the cohesion source and its associated parameters— A for van der Waals induced cohesion, RH for condensed-capillary cohesion, and F_{max} and x_{max} for square-force cohesion—were varied such that a wide range of cohesion levels, as quantified by F_{max} and v_{crit}^2 in the numerators of $Bo_{G,SSF}$ and Ag_{SSF} , respectively, were obtained. The Young's modulus was also varied, leading to further changes in v_{crit}^2 values (Supp Sec S3). Moreover, the shear rate and particle diameter, which appear in the denominator of $Bo_{G,SSF}$ and Ag_{SSF} , were also varied. Figure 3 contains the results from 63 different SSF simulations. Table S5 contains a complete listing of the system conditions examined (inputs), as well as key output variables for the SSF simulations. Aside from $Bo_{G,SSF}$ and Ag_{SSF} , all other dimensionless groups characterizing the SSF system were kept constant: solids fraction $\phi = 0.05$, restitution coefficient $e = 0.97$, and $L/d = 13.78$, where L is the system length and d is the particle diameter.

The results plotted in Figure 3 provide preliminary support for the hypothesis that energy-based descriptions are more appropriate for dilute systems. Namely, the fraction of particles in agglomerates in Figure 3A does not collapse when plotted against $Bo_{G,SSF}$ (Figure 3A). However, in Figure 3B, the fraction of particles in agglomerates collapses when plotted against Ag_{SSF} . Similarly, for the simulated HCS (Figure 4) and riser (Figure 5), and for the experimental BB (Figure 6), collapse is observed against Ag but not Bo_G over a wide range of input parameters. For the simulated dilute systems, e.g., HCS and riser, the cohesive source and magnitude of cohesion were varied by changing the relevant input parameters for each cohesion type: The Hamaker constant for the van der Waals force (Equation (5)), the relative humidity for the condensed-capillary force (Equation (6)), and F_{max} and x_{max} for the square force cohesion (Equation (10)). Additionally, the particle properties E and d were also varied along with the initial temperature (system condition) in the HCS, resulting in a total of 18 different HCS simulations, as overviewed in Table S6. For the riser, in addition to changing the parameters influencing the cohesive magnitude— F_{max} and v_{crit}^2 — $Bo_{G,Riser}$ and Ag_{Riser} were manipulated by varying the particle density, Young's modulus, superficial gas velocity (U), and gas viscosity (μ), for a total of 36 riser conditions that were simulated (Table S7 in supplementary material). The numerator and denominator of $Bo_{G,BB}$ and Ag_{BB} were experimentally varied by using glass beads of different size (Supp. Sec. S2) and adjusting the RH , resulting in BB experiments at 11 different conditions (Table S8 in the supplementary material). Collectively, the collapse of these dilute systems (SSF, HCS, riser, and BB) for Ag and not Bo_G provide robust evidence that systems dominated by brief contacts are most appropriately described by energy-based arguments. A plausible physical explanation is as follows: particles experiencing brief collisions must overcome energy losses associated with cohesion to avoid agglomeration (Figure 1B); such a hysteresis

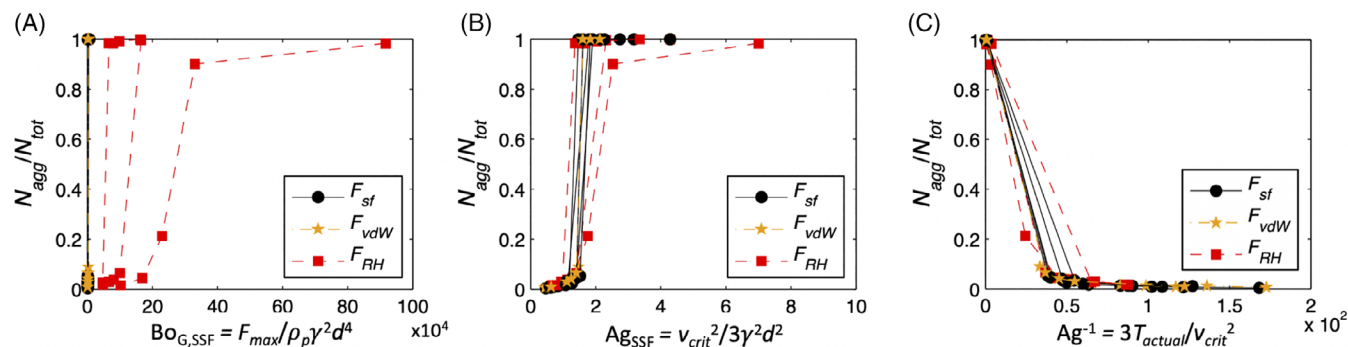


FIGURE 3 Simple shear flow (SSF) simulation: Fraction of particles in agglomerates plotted against (A) $Bo_{G,SSF}$ and (B) Ag_{SSF} . (C) Fraction of particles in agglomerates plotted against $1/Ag$ determined using the measured (output) T_{actual} . The shape and color of the marker indicates the source of cohesion, that is, square-force model (black circle), van der Waals (yellow star), and relative humidity (red square). Along a given line connecting the same type of markers, only the shear rate γ is changed. Different lines denote a given cohesion source (same line type), and are obtained by varying the cohesion magnitude (A for F_{vdW} , RH for F_{RH} , and F_{max} and x_{max} for F_{sf}) and particle properties (E and d). Collectively, results from 63 simulations are plotted; see Supplementary Table S5 for listing of inputs. Dimensionless groups $\phi = 0.05$, $e = 0.97$, and $L/d = 13.78$ were kept constant [Color figure can be viewed at wileyonlinelibrary.com]

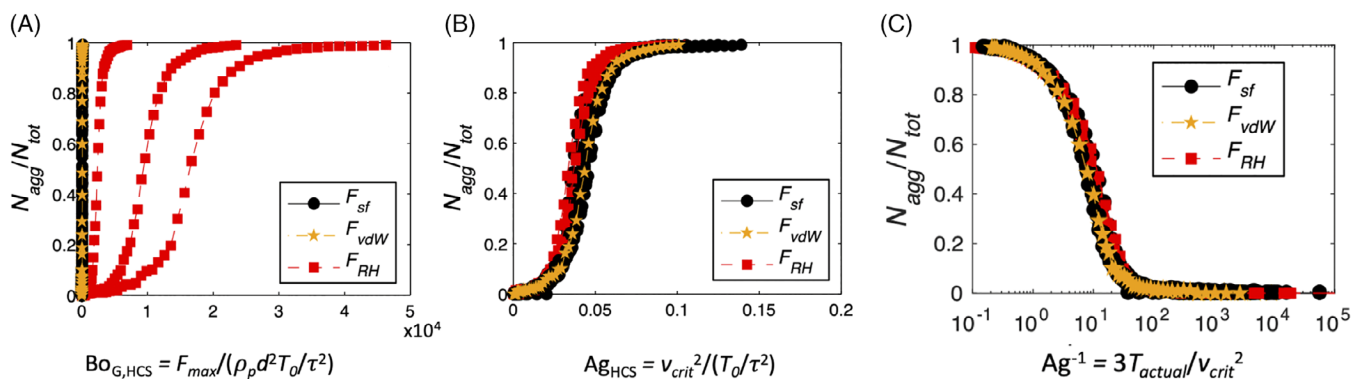


FIGURE 4 Homogenous cooling system (HCS) simulation: Fraction of particles in agglomerates from the simulated HCS plotted against (A) $Bo_{G,HCS}$ and (B) Ag_{HCS} . (C) Fraction of particles in agglomerates plotted against $1/Ag$ determined using the measured (output) T_{actual} . The shape and color of the marker indicates the source of cohesion, that is, square-force model (black circle), van der Waals (yellow star), and relative humidity (red square), and lines only connect data points for the time evolution of HCS simulations with the same particle properties and T_0 . The cohesion source input parameters A , RH , F_{max} , and x_{max} were varied to adjust the cohesion magnitude (i.e., F_{max} and v_{crit}^2) for the van der Waals, condensed-capillary and square-force cohesion sources, respectively. Different lines denote a given cohesion source and T_0 , and were achieved by changing the particle diameter and Young's modulus. Results from HCS simulations run with 18 different conditions are plotted and the full list of conditions are tabulated in the supplemental material Table S6. Dimensionless groups $\phi = 0.05$, $e = 0.97$, and $L/d = 13.78$ were kept constant [Color figure can be viewed at wileyonlinelibrary.com]

(agglomeration upon impact) cannot be captured by the force profile (Figure 1A).

It is also noteworthy that the Ag plots (Figures 3B,4B,5B,6B) in the dilute systems are similar in shape. This similarity can be traced to the transition from non-agglomerating to agglomerating regime that occurs when the KE of particle collisions just balances the KE dissipated during collisions. At this transition point, the systems quickly approach a fully agglomerated state ($N_{agg}/N_{tot} = 1$) once agglomeration onsets as the KE generation becomes smaller than the dissipation.

Despite their similarity in shape, the value of Ag for which the transition from non-agglomerating to agglomerating occurs varies by orders of magnitude for the different systems (Figures 3B,4B,5B,6B). Such differences are a result of the denominator of Ag being

expressed in terms of T_{sys} , a characteristic temperature that is proportional to the granular temperature in a given system rather than a direct estimate of its magnitude (Section 4.1). To further illustrate this point, the granular temperature was extracted from all of the simulated systems (SSF, HCS, and riser)- T_{actual} -and used in the denominator of Ag instead of T_{sys} ; see Figures 3C,4C,5C, respectively. The inverse of Ag is plotted in Figures 3C, 4C, 5C for clarity since $T_{actual} = 0$ when the particles have no relative motion-i.e., the particles have completely agglomerated. Two points are noteworthy when comparing these plots to their 3B, 4B, and 5B counterparts. First, the collapse when using T_{actual} is tighter since the actual (extracted) T values are used in the abscissa rather than a characteristic temperature (T_{sys}) estimated from input parameters. Second, as plotted in Figure 7, for systems with the same value of other dimensionless

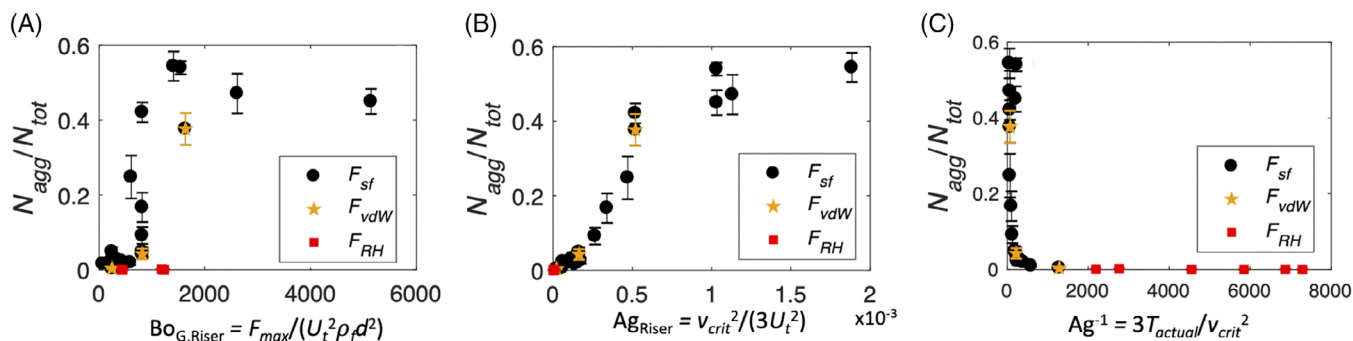


FIGURE 5 Riser simulation: Fraction of particles in agglomerates from the simulated riser plotted against (A) $Bo_{G,Riser}$ and (B) Ag_{Riser} . (C) Fraction of particles in agglomerates plotted against $1/Ag$, which is determined from the measured (output) granular temperature T_{actual} . The shape and color of the marker indicates the source of cohesion, that is, square-force model (black circle), van der Waals (yellow star), and relative humidity (red square). Different riser simulations for the same cohesion source (same marker type) are obtained by varying the cohesion magnitude (A for F_{vdW} , RH for F_{RH} , F_{max} and x_{max} for F_{sf}), and the particle properties (E , and ρ_p) and gas properties (μ and superficial gas velocity). Results from riser simulations run with 36 different conditions are plotted, the conditions for which are provided in a table in the supplemental material Table S7. Dimensionless groups $\phi = 0.01$, $e = 0.97$, and $L/d = 50.5$ were kept constant [Color figure can be viewed at wileyonlinelibrary.com]

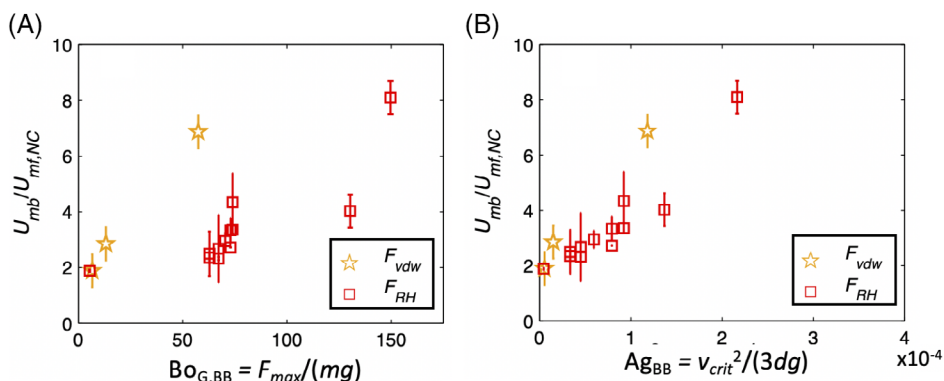


FIGURE 6 Bubbling bed (BB) experiments: U_{mb} measured from BB experiments plotted against (A) $Bo_{G,BB}$ and (B) Ag_{BB} . The color and shape of the marker indicates the source of cohesion, van der Waals (yellow star), and relative humidity (red square), but each data point corresponds to a different set of experimental conditions (e.g., different particle diameter or relative humidity). Measurements with the same cohesion source (same marker type) are obtained by varying the cohesion magnitude (RH for F_{RH}) and particle diameter (d). A detailed list of the experimental conditions associated with the results are listed in a detailed table in the supplemental material (Table S8). Results are plotted from BB experiments run under 11 different conditions [Color figure can be viewed at wileyonlinelibrary.com]

groups, e.g., $\phi = 0.05$, the value of the transitional agglomerate number now overlaps for HCS and SSF.

Note that an *a priori* estimate and inclusion of the proportionality constant between T_{sys} and T_{actual} for each system would thus allow for a direct comparison of magnitudes of Ag , and thus an even more universal description of cohesive systems. Nonetheless, determining this constant of proportionality is non-trivial at best and beyond the scope of this work. Put another way, T_{actual} is an output (dependent variable), but regime maps are only useful in practice if the abscissa is a function of inputs alone (independent variables). The implications of using the characteristic temperature T_{sys} rather than T_{actual} on the generality of regime maps is included in the Summary (Section 5.1).

4.3 | Collapse of enduring contact (dense) systems

Next we consider the behavior of denser systems in which enduring contacts dominate the behavior, to see if they collapse with Bo_G and/or Ag . In the dense PB system, collapse with Bo_G is observed for the porosity in both the experimental (Figure 8A) and simulated (Figure 8B) PB systems; similar plots are not shown for Ag since particles in the PB are static ($T_{sys} = 0$) and thus Ag_{PB} is ill-defined. In Figure 8, a wide range of PB conditions were tested (8 experimental and 21 simulated). For the experimental PB, the source and magnitude of cohesion was varied by changing the humidity level of the fluidized air (van der Waals cohesion dominates at $RH = 0\%$, and capillary condensation becomes

increasing important with increasing RH). In simulations, F_{max} and x_{max} were varied for the square-force model. In both the experiments and simulations, different diameter particles were used, allowing for a larger range of $Bo_{G,PB}$ to be tested. The list of conditions that PB experiments and simulations were performed is provided in Tables S9 and S10, respectively.

Additionally, the normalized discharge rates predicted in the hopper system collapse against $Bo_{G,Hopper}$ but not Ag_{Hopper} , as evidenced in Figure 9. To achieve a range of different $Bo_{G,Hopper}$ and Ag_{Hopper} values, simulations were carried out by varying A for the van der Waals cohesive source, RH for the condensed capillary cohesion source and F_{max} and x_{max} for the square-force cohesion source.

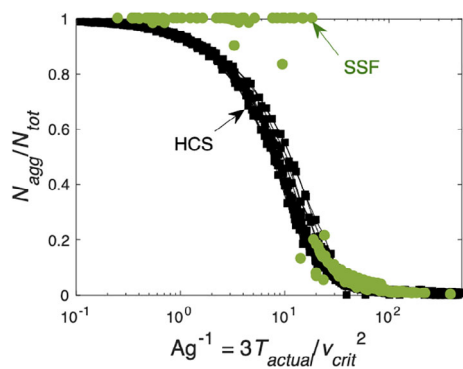


FIGURE 7 Homogenous cooling system (HCS) and simple shear flow (SSF) simulations: fraction of particles in agglomerates plotted against $1/Ag$, which is determined using the actual (measured) granular temperature T_{actual} . The color and shape of the data markers indicates the system, that is, HCS (black squares) or SSF (green circles). Lines only connect data points for the time evolution of HCS transient simulations with the same particle properties and T_o . The simulation results are originally plotted in Figures 3 and 4 and hence the collapse of $1/Ag$ for two systems is found for a wide range of simulation input conditions. Dimensionless groups $\phi = 0.05$, $e = 0.97$, and $L/d = 13.78$ for both the HCS and SSF were kept constant [Color figure can be viewed at wileyonlinelibrary.com]

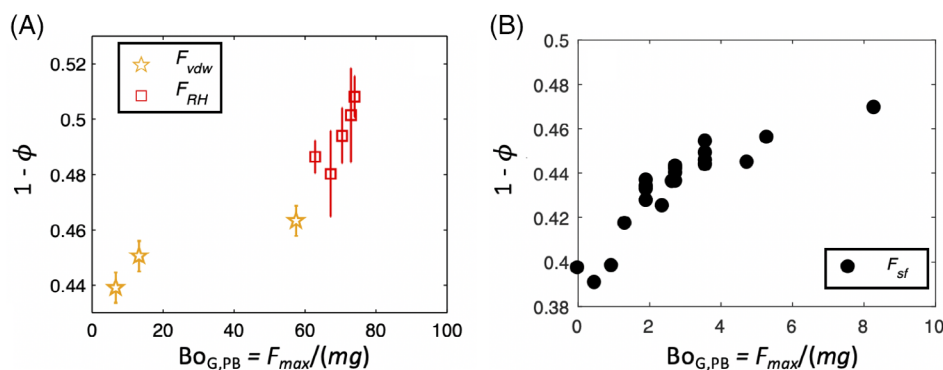


FIGURE 8 Packed bed (PB) experiment and simulations: Porosity plotted against $Bo_{G,PB}$ for the (A) experimental and (B) simulated systems. The color and shape of the marker indicates the source of cohesion, namely, van der Waals (yellow star), relative humidity (red square), and square-force cohesion (black circles). Each data point corresponds to a different set of conditions that are listed in detail in Table S9 (experiment) and Table S10 (DEM) in the supplemental material. Results from eight different PB experimental conditions are plotted in (A) and 21 different PB simulations in (B) [Color figure can be viewed at wileyonlinelibrary.com]

Moreover, the particle density and Young's modulus were changed in order to further vary $Bo_{G,Hopper}$ and Ag_{Hopper} . A full listing of the input parameters for the simulations is provided in Table S11 in the supplemental material.

Collectively, collapse of the dependent variable of interest against Bo_G but not Ag in these dense systems indicates that force is the appropriate micro-scale cohesive quantity for understanding the macro-scale behavior as opposed to energy. A plausible physical explanation is as follows: particles with enduring contacts need to overcome the maximum cohesive force, which occurs at contact (i.e., Figure 1A), to induce relative (normal) motion; the concept of agglomeration versus de-agglomeration (Figure 1B) based on energy arguments is ill-defined in dense flows where contacts are enduring in nature.

4.4 | Revisiting Geldart's chart

It is worth noting that the results described here may seem inconsistent with previous work on Geldart's chart¹⁸ in which collapse with Bo_G (force-dominated) at the Group A/B border was found for a system that we report to collapse with Ag (energy-dominated)—namely, the bubbling bed experiments in Figure 6. For the case of van der Waals forces only, this collapse with Bo_G is fortuitous because an increase in F_{max} is linearly correlated to an increase in v_{crit}^2 for van der Waals forces (numerators of Bo_G and Ag , respectively). In particular, consider a simple approximation of the F_{vdw} theory, i.e.,

$$F_{vdw} \approx Ar_s/(12x^2), \quad (22)$$

using this approximation in conjunction with Equation (1), the corresponding cohesive energy is obtained, namely $W_{vdw} = -Ar_s/(12x)$. Accordingly, from Equation (2), an analytical expression for the critical agglomeration velocity can be found:

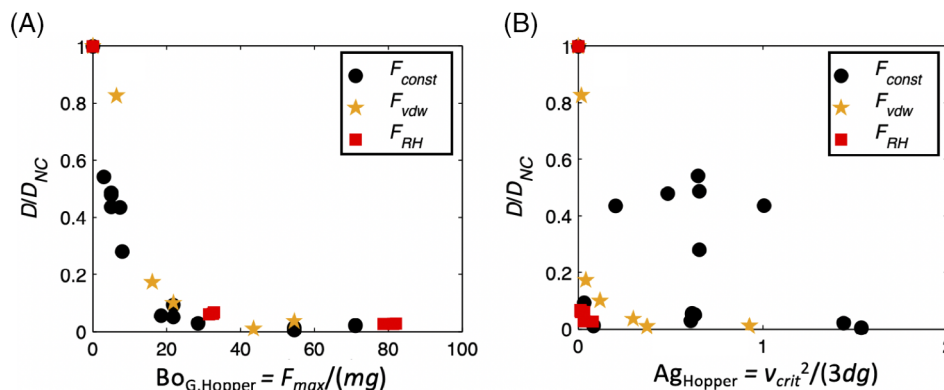


FIGURE 9 Hopper simulations: Normalized discharge rate of particles from the simulated hopper plotted against (A) $Bo_{G,Hopper}$ and (B) Ag_{Hopper} . The color and shape of the marker indicates the source of cohesion, namely, square-force model (black circle), van der Waals (yellow star), and relative humidity (red square), where each data point corresponds to a different set of hopper conditions that are listed in a detailed table in the supplemental material Table S11. Each data point corresponds to a different set of conditions (e.g., different Young's modulus, or particle density). Results from hopper simulations run with 21 different conditions are plotted [Color figure can be viewed at wileyonlinelibrary.com]

$$v_{crit,vdW}^2 \approx \frac{Ar_s}{6} \left(\frac{1}{x_{min}} - \frac{1}{x_{max}} \right) \frac{(1-e^2)}{me^2}. \quad (23)$$

From Equations (22) and (23), it is seen that $F_{vdW,max}$ ($= F_{vdW}(x = x_{min})$) and $v_{crit,vdW}^2$ are proportional to Ar_s and Ar_s/m , respectively, and thus the two numerators for Bo_G and Ag , namely $F_{vdW,max}$ and $KE_{crit,vdW}$ are proportional to one another—i.e., $F_{max} \propto KE_{crit} \propto Ar_s$, $F_{max} \propto KE_{crit} \propto Ar_s$. Hence, a given system with van der Waals forces that collapses with Ag will also collapse with Bo_G , and vice versa (see Equations (3) and (4)). This provides an explanation as to why Geldart's chart for fluidized bed (collision dominated), where van der Waals cohesion plays a role in the demarcation between groups C (cohesive), A (mildly-cohesive) and B (non-cohesive) collapses with Bo_G . Note in Figures 3–6, when looking at van der Waals forces only, collapse exists with Bo_G in addition to Ag , which is further support that F_{max} is proportional to KE_{crit} for van der Waals forces only.

4.5 | Changes in other dimensionless groups

The (dimensionless) dependent variables of a system are a function of all relevant dimensionless groups for that system. Although the focus of the current work is on correctly identifying Ag or Bo_G as the appropriate dimensionless group that characterizes cohesion in a given system, there are other dimensionless groups that will impact the dependent variables—restitution coefficient e , etc. To demonstrate the robustness of the reported results, here we show the collapse of Ag or Bo_G is also observed at different fixed values of other dimensionless groups that characterize the HCS system.

Figure 10 illustrates this robustness for HCS at a different solids volume fraction ϕ (Figure 10A,B) and a different restitution coefficient e (Figure 10C,D). In Figure 10, the data markers are used to distinguish data from simulations with different fixed values of ϕ and e . However, for the simulations with a given ϕ and e , the denominators of $Bo_{G,HCS}$

and Ag_{HCS} were varied by changing T_o and t , and the numerators were adjusted by using different sources of cohesion and different cohesion magnitudes (see supplemental material Table S6 for full listing). Collapse of N_{agg}/N_{tot} for different (fixed) values of ϕ (Figure 10A,B) and e (Figure 10C,D) is not expected since ϕ and e belong to the set of dimensionless groups (like Ag or Bo_G) that characterize the system. However, for any given fixed value of ϕ and e (i.e., identical data markers), N_{agg}/N_{tot} collapses with Ag_{HCS} but not with $Bo_{G,HCS}$. Accordingly, the results presented above appear robust, as collapse is observed for Ag only for each constant pairing of e and ϕ considered.

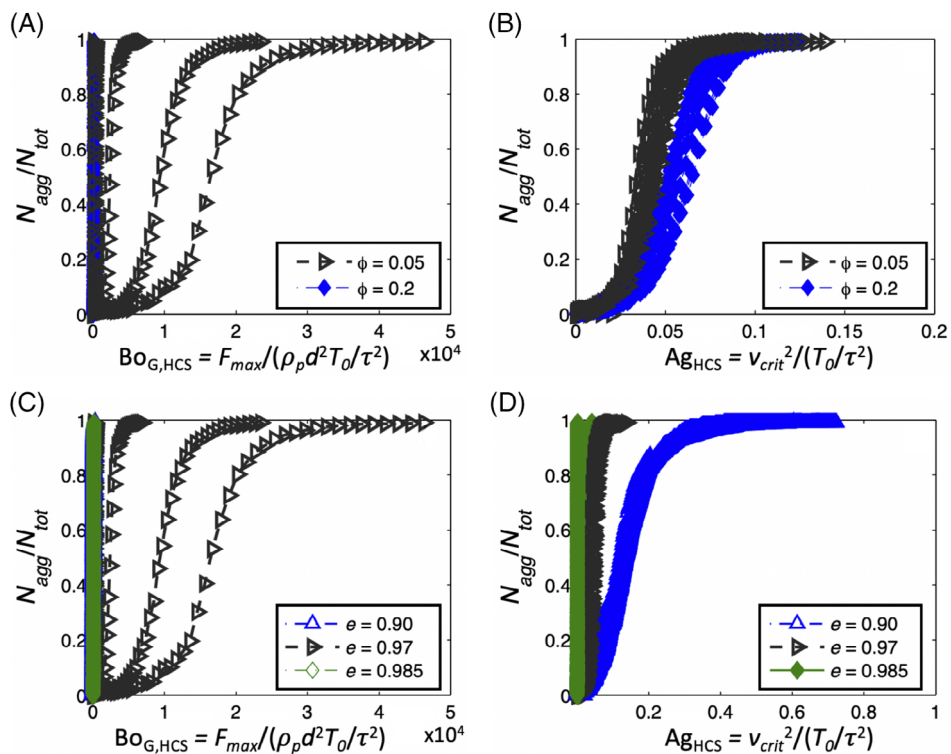
5 | CONCLUDING REMARKS

5.1 | Summary

A long-standing point of debate in cohesive-particle systems is whether a force-based or energy-based description of particle interactions is more appropriate. Estimates of agglomerate size,^{19,55–57} constitutive relations for source terms in populations balances,^{24,58–63} and regime maps^{15,26,62,64–69} are a few prominent examples in which both force- and energy-based descriptions have appeared in the literature, without justification as to why one is more appropriate than the other. Here we aim to decipher the force versus energy conundrum.

We hypothesize that force-based considerations are more appropriate for enduring-contact (“dense”) systems and energy-based considerations are more appropriate for systems with brief contacts (“dilute”). The physical rationale is as follows: systems with sustained contacts (force chains) between particles must overcome a cohesive force to induce relative motion, so a force (momentum) balance is appropriate. Systems with brief (collisional) contacts must overcome energy losses associated with cohesion (in addition to non-cohesive losses like inelasticity) to avoid agglomeration, so an energy balance is appropriate. To test this hypothesis, experiments and simulations were

FIGURE 10 Homogenous cooling system (HCS) simulations: fraction of particles in agglomerates for different solids volume fractions (dimensionless group) values of $\phi = 0.05$ (black) and $\phi = 0.2$ (blue) for increasing (A) $Bo_{G,HCS}$ and (B) Ag_{HCS} ($e = 0.97$); fraction of particles in agglomerates for different coefficient of restitution (dimensionless group) values of $e = 0.90$ (blue), $e = 0.97$ (black), and $e = 0.985$ (green), on the fraction of particles in agglomerates with increasing (C) $Bo_{G,HCS}$ and (D) Ag_{HCS} ($\phi = 0.05$). Dimensionless groups $e = 0.97$, and $L/d = 13.78$ were kept constant in (A) and (B). In (C) and (D), the dimensionless groups $\phi = 0.05$, and $L/d = 13.78$ were kept constant [Color figure can be viewed at wileyonlinelibrary.com]



performed for a wide range of systems (simple shear flow, homogeneous cooling, riser, bubbling fluidized bed, packed bed, and hopper flow) experiencing different types of cohesion (van der Waals, capillary bridges, and square-force); both material properties and system conditions were systematically varied. For a given system, the dimensionless, dependent variable was plotted against two dimensionless numbers indicative of cohesion levels—a generalized bond number Bo_G , which is the ratio of maximum cohesive force to the force driving flow, and a new Agglomerate number Ag , which is the ratio of critical cohesive energy for agglomeration to a characteristic granular energy for the system. The resulting plots showed collapse of the dense systems with Bo_G but not Ag , and vice versa for the dilute systems, thereby providing robust support for the hypothesis.

5.2 | Implications: Regime maps

Regime maps for cohesive-particle flows have been a mainstay in industry for the prediction of various unit operations.^{10,13–15,26,62,64–70} The generality (or lack thereof) of a given regime map depends on what quantities are being plotted. For example, Geldart's¹⁰ chart is developed for fluidized beds at ambient conditions with van der Waals forces as the only possible source of cohesion. Application of Geldart's¹⁰ chart to a fluidized bed operating at non-ambient temperatures or pressures, or application to a different apparatus (e.g., rotating tumbler) is not appropriate. Generally speaking, while system-specific nature of a regime map is difficult to overcome, its application to other material properties, operating conditions and/or sources of cohesion is possible via the use of appropriate

dimensionless groups. Consider another well-known example—the laminar-to-turbulent transition in single-phase flow as characterized by the Reynolds number (Re). The definition of the Reynolds number is broadly defined as the ratio of the inertial to viscous stresses in a fluid flow field or $Re = \rho_f UL_{sys}/\mu$ (not system specific), but the explicit form of the Reynolds number is system specific as it depends on the length scale L_{sys} relevant to the particular system geometry, for example, diameter D of a circular pipe ($Re_{pipe} = \rho_f UD/\mu$), length along a flat plate L_p for boundary layer flow ($Re_{plate} = \rho_f UL_p/\mu$), and particle diameter for flow of a spherical particle ($Re_{particle} = \rho_f Ud/\mu$). For circular pipes, the critical value of Re demarcating laminar and turbulent flow regimes is $Re_{crit,pipe} \sim 2100$. Any changes to material properties, characteristic velocity or system dimensions are reflected in the value Re being compared to Re_{crit} , whereas the value of Re_{crit} itself (the regime map) only changes if the system geometry changes (circular pipe, square pipe, flow over flat plate, etc.). Similar to Re , our definitions of Bo_G (Equation (3)) and Ag (Equation (4)) are broadly defined for any system, and thus the explicit form for a specific system depends on input variables corresponding to the given system. Furthermore, it is worthwhile to note that Bo_G and Ag are just two of the dimensionless groups making up a full dimensionless set for a given system and that this full set is not unique; for example, an equivalent set can be formed via multiplication of one dimensionless group by another, and replacement of the original group by said product.

The findings reported here are critical for building more universal regime maps—ones that are independent of cohesion source, as well as material properties and operating conditions. Our results indicate that two pertinent dimensionless groups for cohesion are Bo_G and Ag : Bo_G (force-based) is appropriate for systems with enduring collisions

only (dense), Ag (energy-based) is appropriate for systems with brief collisions only (dilute), and both Bo_G and Ag are necessary for systems in which both types of contacts are present. There are likely numerous other dimensionless groups needed to fully characterize a given system (solids fraction, restitution coefficient, density ratio, etc.) which are not related to cohesion, and hence not the focus of this work. Similarly, unlike the monodisperse systems considered here, more complex systems would lead to even more dimensionless groups (size ratio, particle size distribution, etc.).

As alluded to above, future regime maps based on Bo_G and/or Ag will be system-dependent, similar to the geometry-specific nature of the form and critical Reynolds number for the laminar-turbulent transition of single-phase flows (circular pipe, square pipe, flow over flat plate, etc.). However, when presented in dimensionless form, the regime maps will be applicable to different types of cohesion, materials, and operating conditions. The applicability of a given Bo_G -and/or Ag-based regime map to different types of cohesion (van der Waals, capillary bridges, etc.) is a particularly novel aspect of this work, representing a considerable step toward a more general description of cohesive systems.

5.3 | Implications: Particle-level cohesion model and determination of F_{\max} and v_{crit}^2

To construct regime maps, an estimate of F_{\max} or v_{crit}^2 is required for the numerators of Bo_G (Equation (3)) and Ag (Equation (4)), respectively. In this work, estimates for these quantities were based on complex, rigorous force models for van der Waals forces (Equation (5)) and humidity effects (Table 2). Such particle cohesion models can take years to develop and validate,^{21,35,42} which leads to two practical questions: (i) what is the minimal, yet sufficient, physics needed in such a model? (ii) Can the corresponding model parameters be extracted from a simple bulk experiment?

Regarding (i), the results obtained here suggest that the simplest form of a particle cohesion model should be one which maintains the characteristic force (F_{\max}) and energy (mv_{crit}^2) of cohesion, as all of the systems considered here collapsed with Bo_G or Ag. Such a “square-force” model—one in which a constant force occurs at small separation distances and then drops to zero at a specified cutoff distance (Equation (10))—was proposed recently by Liu et al.³⁰ In their work, the constant force in the square-force model was set equal to F_{\max} of more rigorous models, and the cutoff distance was chosen such that area under the curve equals the critical cohesion energy, or mv_{crit}^2 , of the more rigorous models. DEM simulations of both dilute and dense many-particle systems showed that the resulting square-force model compares well with more rigorous forms of cohesion models, thereby providing initial validation for the square-force approach.³⁰

Regarding (ii), the parameters for this simplified, square-force model of particle cohesion can be extracted in straightforward manner for lightly cohesive particles, as described recently by Liu et al.³⁰ In particular, the defluidization curve of a fluidized bed (pressure drop vs. gas velocity) was used in conjunction with DEM simulations to

determine F_{\max} and the cutoff distance (and hence v_{crit}) in a sequential manner designed to isolate their effects. Extension to more cohesive particles is currently underway via the use of a commercial rheometer.⁷¹ Such straightforward bulk experiments that can be used to extract the parameters of the square-force model represent a much-needed alternative to the protracted development of more rigorous, and unnecessarily complex, cohesion models.

5.4 | Implications: DEM simulations

As described above, the square-force model captures all that is needed in a simplified model of cohesion, namely the characteristic force and energy, to correctly predict interactions among cohesive particles. Although a more rigorous description (e.g., Equation (5) for van der Waals forces) is capable of providing a more accurate force vs. separation distance curve, the results obtained here and prior results³⁰ indicate that such complexity is not required for purposes of DEM simulations.

5.5 | Implications: Continuum theory

The results obtained here provide an answer to the longstanding question as to whether force-based^{55,56} or energy-based^{24,58,59} closures to population balances are more appropriate. Specifically, a continuum theory capable of predicting the behavior of cohesive particles requires consideration of F_{\max} (force) for dense systems and v_{crit}^2 (energy) for dilute flows, or both for flows with both enduring and short (nearly-instantaneous) contacts. The two concentration limits can be unified via the radial distribution function $g_o(\phi, x)$ —i.e.,

$$\lim_{\phi \rightarrow \phi_{\max}} \frac{\int_0^{\phi_{\max}} F_c(x) g_o(\phi, x) dx}{\int_0^{\phi_{\max}} g_o(\phi, x) dx} = F_{\max} \quad \text{in the limit of dense flows, and}$$

$$\lim_{\phi \rightarrow 0} \frac{\int_0^{\phi_{\max}} F_c(x) g_o(\phi, x) dx}{\int_0^{\phi_{\max}} g_o(\phi, x) dx} = \frac{W}{x_{\max}} \quad \text{for dilute.}$$

ACKNOWLEDGMENTS

The authors are grateful to Dow Corning Corporation for providing the funding for this work. This work utilized the RMACC Summit supercomputer, which is supported by the National Science Foundation (awards ACI-1532235 and ACI-1532236), the University of Colorado Boulder, and Colorado State University. The Summit supercomputer is a joint effort of the University of Colorado Boulder and Colorado State University. Additionally, the authors would like to thank Andrew Miller, Kacey Paulin, and Haley Manchester for their efforts conducting experiments.

AUTHOR CONTRIBUTIONS

Wyatt Casey LaMarche: Conceptualization; formal analysis; investigation; writing-original draft; writing-review & editing. **Peiyuan Liu:** Formal analysis; investigation; software; writing-review & editing. **Kevin Kellogg:** Formal analysis; investigation; writing-review & editing. **Aaron Lattanzi:** Formal analysis; writing-review & editing. **Christine Hrenya:**

Formal analysis; funding acquisition; project administration; resources; supervision; writing-original draft; writing-review & editing.

DATA AVAILABILITY STATEMENT

The data that support the findings of this study are available from the corresponding author upon reasonable request.

ORCID

W. Casey Q. LaMarche  <https://orcid.org/0000-0002-6197-5747>

REFERENCES

- Blum J. Laboratory experiments on preplanetary dust aggregation. *Space Sci Rev.* 2000;92(1):265-278.
- Rozitis B, MacLennan E, Emery JP. Cohesive forces prevent the rotational breakup of rubble-pile asteroid (29075) 1950 DA. *Nature.* 2014;512(7513):174-176. <http://dx.doi.org/10.1038/nature13632>.
- Shi D, Abatan AA, Vargas WL, McCarthy JJ. Eliminating segregation in free-surface flows of particles. *Phys Rev Lett.* 2007;99(14):148001.
- Zhang P, Law CK. An analysis of head-on droplet collision with large deformation in gaseous medium. *Phys Fluids.* 2011;23(4):042102.
- Veen SJ, Antoniuk O, Weber B, Potenza MAC, Mazzoni S, Schall P, Wegdam GH. Colloidal aggregation in microgravity by critical casimir forces. *Physical Review Letters.* 2012;109(24):248302. <http://dx.doi.org/10.1103/physrevlett.109.248302>.
- Urvoy A, Ripka F, Lesanovsky I, Booth D, Shaffer JP, Pfau T, Löw R. Strongly correlated growth of Rydberg aggregates in a vapor cell. *Physical Review Letters.* 2015;114(20):203002. <http://dx.doi.org/10.1103/physrevlett.114.203002>.
- Chew JW, Cahyadi A, Hrenya CM, Karri R, Cocco RA. Review of entrainment correlations in gas-solid fluidization. *Chem Eng J.* 2015; 260:152-171.
- Cahyadi A, Neumayer AH, Hrenya CM, Cocco RA, Chew JW. Comparative study of transport disengaging height (TDH) correlations in gas-solid fluidization. *Powder Technol.* 2015;275:220-238.
- Shabanian J, Jafari R, Chaouki J. Fluidization of ultrafine powders. *Int Rev Chem Eng.* 2012;4(1):16-50.
- Geldart D. Types of gas fluidization. *Powder Technol.* 1973;7(5): 285-292.
- Valverde JM, Castellanos A. Types of gas fluidization of cohesive granular materials. *Phys Rev E.* 2007;75(3):031306.
- Castellanos A, Valverde JM, Quintanilla MAS. Physics of compaction of fine cohesive particles. *Phys Rev Lett.* 2005;94(7):075501.
- Li H, McCarthy JJ. Phase diagrams for cohesive particle mixing and segregation. *Phys Rev E.* 2005;71:021305.
- Jain K, Shi D, McCarthy JJ. Discrete characterization of cohesion in gas-solid flows. *Powder Technol.* 2004;146(1-2):160-167.
- Nase ST, Vargas WL, Abatan AA, McCarthy JJ. Discrete characterization tools for cohesive granular material. *Powder Technol.* 2001;116 (2-3):214-223.
- Trappe V, Prasad V, Cipelletti L, Segre PN, Weitz DA. Jamming phase diagram for attractive particles. *Nature.* 2001;411(6839):772-775.
- Web of Science, Accessed Feb. 8, 2020.
- Molerus O. Interpretation of Geldart's type a, B, C and D powders by taking into account interparticle cohesion forces. *Powder Technol.* 1982;33(1):81-87.
- Forsyth AJ, Hutton SR, Osborne CF, Rhodes MJ. Effects of interparticle force on the packing of spherical granular material. *Phys Rev Lett.* 2001;87(24):244301.
- Forsyth AJ, Hutton SR, Rhodes MJ, Osborne CF. Effect of applied interparticle force on the static and dynamic angles of repose of spherical granular material. *Phys Rev E.* 2001;63(3):031302.
- LaMarche CQ, Miller AW, Liu P, Hrenya CM. Linking micro-scale predictions of capillary forces to macro-scale fluidization experiments in humid environments. *AIChE J.* 2016;62(10):3585-3597.
- Dahneke B. The capture of aerosol particles by surfaces. *J Colloid Interface Sci.* 1971;37(2):342-353.
- Castellanos A, Valverde JM, Quintanilla MAS. Aggregation and sedimentation in gas-fluidized beds of cohesive powders. *Phys Rev E.* 2001;64(4):041304.
- Kantak AA, Hrenya CM, Davis RH. Initial rates of aggregation for dilute, granular flows of wet particles. *Phys Fluids.* 2009;21(2):023301.
- Shabanian J, Duchesne MA, Runstedtler A, Syamlal M, Hughes RW. Improved analytical energy balance model for evaluating agglomeration from a binary collision of identical wet particles. *Chem Eng Sci.* 2020;223:115738.
- Strauch S, Herminghaus S. Wet granular matter: a truly complex fluid. *Soft Matter.* 2012;8(32):8271-8280.
- Israelachvili JN. *Intermolecular and Surface Forces.* 3rd ed. Boston: Academic Press; 2011.
- Seville JPK, Tüzün U, Clift R. *Processing of Particulate Solids.* New York: Chapman & Hall; 1997.
- Fingerle A, Roeller K, Huang K, Herminghaus S. Phase transitions far from equilibrium in wet granular matter. *New J Phys.* 2008;10(5):053020.
- Liu P, LaMarche CQ, Kellogg KM, Hrenya CM. A square-force cohesion model and its extraction from bulk measurements. *AIChE J.* 2018; 64(7):2329-2339.
- Foerster SF, Louge MY, Chang H, Allia K. Measurements of the collision properties of small spheres. *Phys Fluids.* 1994;6(3):1108-1115.
- Kobayashi T, Tanaka T, Shimada N, Kawaguchi T. DEM-CFD analysis of fluidization behavior of Geldart group a particles using a dynamic adhesion force model. *Powder Technol.* 2013;248:143-152.
- Gu Y, Ozel A, Sundaresan S. A modified cohesion model for CFD-DEM simulations of fluidization. *Powder Technol.* 2016;296:17-28.
- Liu P, LaMarche CQ, Kellogg KM, Hrenya CM. Fine-particle defluidization: interaction between cohesion, Young's modulus and static bed height. *Chem Eng Sci.* 2016;145:266-278.
- LaMarche CQ, Leadley S, Liu P, Kellogg KM, Hrenya CM. Method of quantifying surface roughness for accurate adhesive force predictions. *Chem Eng Sci.* 2017;158:140-153.
- Liu P, LaMarche CQ, Kellogg KM, Leadley S, Hrenya CM. Cohesive grains: bridging microlevel measurements to macrolevel flow behavior via surface roughness. *AIChE J.* 2016;62(10):3529-3537.
- Rabinovich YI, Adler JJ, Ata A, Singh RK, Moudgil BM. Adhesion between nanoscale rough surfaces I. role of asperity geometry. *J Colloid Interface Sci.* 2000;232(1):10-16.
- Rabinovich YI, Adler JJ, Ata A, Singh RK, Moudgil BM. Adhesion between nanoscale rough surfaces II. Measurement and comparison with theory. *J Colloid Interface Sci.* 2000;232(1):17-24.
- Orr FM, Scriven LE, Rivas AP. Pendular rings between solids: meniscus properties and capillary force. *J Fluid Mech.* 1975;67(4):723-742.
- Butt H-J, Graf K, Kappl M. *Physics and Chemistry of Interfaces.* 1st ed. Weinheim, Germany: Wiley-VCH; 2003.
- Pierrat P, Caram HS. Tensile strength of wet granular materials. *Powder Technol.* 1997;91:83-93.
- LaMarche CQ, Miller AW, Liu P, Leadley S, Hrenya CM. How nanoscale roughness impacts the flow of grains influenced by capillary cohesion. *AIChE Journal.* 2017;63(12):5250-5257. <http://dx.doi.org/10.1002/aic.15830>.
- Xiao X, Qian L. Investigation of humidity-dependent capillary force. *Langmuir.* 2000;16(21):8153-8158.
- Butt H-J, Kappl M. Normal capillary forces. *Adv Colloid Interface Sci.* 2009;146(1-2):48-60.
- Weber MW, Hoffman DK, Hrenya CM. Discrete-particle simulations of cohesive granular flow using a square-well potential. *Granul Matter.* 2004;6(4):239-254.

46. Campbell CS. Stress tensor for simple shear flows of a granular material. *J Fluid Mech.* 1989;203:449-473.
47. Bagnold RA. Experiments on a gravity-free dispersion of large solid spheres in a Newtonian fluid under shear. *Proc R Soc London, Ser A.* 1954;255(1160):49-63.
48. Fullmer WD, Hrenya CM. The clustering instability in rapid granular and gas-solid flows. *Annu Rev Fluid Mech.* 2017;49(1):485-510.
49. Haff PK. Grain flow as a fluid-mechanical phenomenon. *J Fluid Mech.* 1983;134:401-430.
50. Garzó V. Instabilities in a free granular fluid described by the Enskog equation. *Phys Rev E.* 2005;72(2):021106.
51. Rhodes M. *Introduction to Particle Technology.* 2nd ed. Chichester: John Wiley & Sons; 2008.
52. Garzó V, Tenneti S, Subramaniam S, Hrenya CM. Enskog kinetic theory for monodisperse gas–solid flows. *J Fluid Mech.* 2012;712:129-168.
53. LaMarche CQ, Liu P, Kellogg KM, Hrenya CM. Fluidized-bed measurements of carefully-characterized, mildly-cohesive (Group A) particles. *Chem Eng J.* 2017;310(1):259-271.
54. Tsinontides SC, Jackson R. The mechanics of gas fluidized beds with an interval of stable fluidization. *J Fluid Mech.* 1993;255:237-274.
55. van Wachem B, Sasic S. Derivation, simulation and validation of a cohesive particle flow CFD model. *AIChE J.* 2008;54(1):9-19.
56. Motlagh AHA, Grace JR, Salcudean M, Hrenya CM. New structure-based model for Eulerian simulation of hydrodynamics in gas–solid fluidized beds of Geldart group “A” particles. *Chem Eng Sci.* 2014;120:22-36.
57. Zhou T, Li H, Shinohara K. Agglomerating fluidization of group C particles: major factors of coalescence and breakup of agglomerates. *Adv Powder Technol.* 2006;17(2):159-166.
58. Liu L. Kinetic theory of aggregation in granular flow. *AIChE J.* 2011;57(12):3331-3343.
59. Kellogg KM, Liu P, LaMarche CQ, Hrenya CM. Continuum theory for rapid cohesive-particle flows: general balance equations and discrete-element-method-based closure of cohesion-specific quantities. *J Fluid Mech.* 2017;832:345-382.
60. Sun L, Luo K, Fan J. Population balance equation of cohesive particle flow in a circulating fluidized bed. *Chem Eng Technol.* 2017;40(9):1544-1551.
61. Sun L, Yu W, Hassan M, Wang S, Liu G, Lu H. Investigation of aggregation kernel and simulation of cohesive particle flow. *Chem Eng Technol.* 2016;39(10):1858-1866.
62. Castellanos A, Valverde JM, Pérez AT, Ramos A, Watson PK. Flow regimes in fine cohesive powders. *Phys Rev Lett.* 1999;82(6):1156.
63. Nanni NR, Peglow M, Warnecke G, Kumar J, Heinrich S, Kuipers JAM. Modeling of aggregation kernels for fluidized beds using discrete particle model simulations. *Particuology.* 2014;13(Suppl C):134-144.
64. Liu D, van Wachem BGM, Mudde RF, Chen X, van Ommen JR. An adhesive CFD-DEM model for simulating nanoparticle agglomerate fluidization. *AIChE J.* 2016;62(7):2259-2270.
65. Shi H, Roy S, Weinhart T, Magnanimo V, Luding S. Steady state rheology of homogeneous and inhomogeneous cohesive granular materials. *Granul Matter.* 2019;22:14.
66. Gonzalez S, Thornton AR, Luding S. Free cooling phase-diagram of hard-spheres with short- and long-range interactions. *Eur Phys J Spec Top.* 2014;223(11):2205-2225.
67. Jarray A, Shi H, Scheper BJ, Habibi M, Luding S. Cohesion-driven mixing and segregation of dry granular media. *Sci Rep.* 2019;9(1):13480.
68. Girardi M, Radl S, Sundaresan S. Simulating wet gas–solid fluidized beds using coarse-grid CFD-DEM. *Chem Eng Sci.* 2016;144:224-238.
69. van Wachem B, Thalberg K, Nguyen D, de JL M, Rummelgas J, Niklasson-Bjorn I. Analysis, modelling and simulation of the fragmentation of agglomerates. *Chem Eng Sci.* 2020;227:115944.
70. Pohl S, Kleinebudde P. A review of regime maps for granulation. *Int J Pharm.* 2020;587:119660.
71. Mishra I, Liu P, Shetty A, Hrenya CM. On the use of a powder rheometer to probe defluidization of cohesive particles. *Chem Eng Sci.* 2020;214:115422.

SUPPORTING INFORMATION

Additional supporting information may be found online in the Supporting Information section at the end of this article.

How to cite this article: LaMarche WCQ, Liu P, Kellogg KM, Lattanzi AM, Hrenya CM. Toward general regime maps for cohesive-particle flows: Force versus energy-based descriptions and relevant dimensionless groups. *AIChE J.* 2021; 67(9):e17337. <https://doi.org/10.1002/aic.17337>